AGU PUBLICATIONS

JGR

Journal of Geophysical Research: Solid Earth

RESEARCH ARTICLE

10.1002/2013JB010793

Key Points:
- Electrical anomalies can be observed during frictional stick-slip events
- We suggest that electron hole migration is the electrical charging mechanism
- Granular theory and electrical mechanisms may provide EQ early warning signal

Correspondence to:
J. R. Leeman,
jleeman@psu.edu

Citation:
Leeman, J. R., M. M. Scuderi, C. Marone, D. M. Saffer, and T. Shinbrot (2014), On the origin and evolution of electrical signals during frictional stick slip in sheared granular material, *J. Geophys. Res. Solid Earth*, *119*, 4253–4268, doi:10.1002/2013JB010793.

Received 28 OCT 2013
Accepted 14 APR 2014
Accepted article online 17 APR 2014
Published online 9 MAY 2014

On the origin and evolution of electrical signals during frictional stick slip in sheared granular material

J. R. Leeman[1], M. M. Scuderi[1], C. Marone[1], D. M. Saffer[1], and T. Shinbrot[2]

[1]Rock and Sediment Mechanics Laboratory, Department of Geosciences, Pennsylvania State University, University Park, Pennsylvania, USA, [2]Department of Biomedical Engineering, Rutgers University, Piscataway, New Jersey, USA

Abstract Electromagnetic signals have been reported in association with geophysical phenomena including earthquakes, landslides, and volcanic events. Mechanisms that suggested to explain seismoelectrical signals include triboelectricity, piezoelectricity, streaming potentials, and the migration of electron holes, yet the origin of such phenomena remains poorly understood. We present results from laboratory experiments regarding the relationship between electrical and mechanical signals for frictional stick-slip events in sheared soda-lime glass bead layers. The results are interpreted in the context of lattice defect migration and granular force chain mechanics. During stick-slip events, we observe two distinct behaviors delineated by the attainment of a frictional stick-slip steady state. During initial shear loading, layers charge during stick-slip events and the potential of the system rises. After steady state stick-slip behavior is attained, the system begins to discharge. Coseismic signals are characterized by potential drops superimposed on a longer-term trend. We suggest that the observed signal is a convolution of two effects: charging of the forcing blocks and signals associated with the stress state of the material. The long-term charging of the blocks is accomplished by grain boundary movement during the initial establishment of force chain networks. Short-term signals associated with stick-slip events may originate from produced electron holes. Applied to tectonic faults, our results suggest that electrical signals generated during frictional failure may provide a way to monitor stress and the onset of earthquake rupture. Potential changes could produce detectable signals that may forecast the early stages of failure, providing a modest warning of the event.

1. Introduction

A number of electromagnetic signals have been observed during tectonic faulting and mechanical failure of rocks, but the mechanisms underlying these phenomena are still unclear. Recently, efforts to couple observations by the physics and materials science communities with observations of natural phenomena in the geoscience community have begun to show promise [*Enomoto and Zheng*, 1998; *Balk et al.*, 2009; *Takeuchi et al.*, 2010; *Freund*, 2010; *Onuma et al.*, 2011; *Shinbrot et al.*, 2012]. Existing studies indicate that large earthquakes are, in some cases, preceded or accompanied by ultralow frequency electromagnetic emissions, residual magnetic anomalies, and even visible electrical atmospheric discharges known as "earthquake lights" [*Derr*, 1973; *Park et al.*, 1993; *Uyeda et al.*, 2009]. Understanding these phenomena may improve our ability to provide early warning of seismic events or other hazardous material failures and will provide insight into fault zone physical processes and stress conditions during the seismic cycle.

Several mechanisms have been proposed to explain the generation of electrical potentials in Earth, including piezoelectric effects, streaming potential, contact electrification/triboelectrification, fracto-emission, plasma excitation, and semiconductor-like effects [*Finkelstein et al.*, 1973; *Dickinson*, 1982; *Dickinson et al.*, 1982, 1984; *Freund*, 2000; *Frid et al.*, 2000; *Jouniaux and Ishido*, 2013; *Takeuchi and Nagao*, 2013]. Even with an assumed mechanism of charging, there are still many mysterious aspects of the phenomenon, including conduction of the charge to the surface, charge residence time, and earth-atmosphere interaction. Here we examine electrical potentials observed for sheared granular layers that exhibit regular frictional stick-slip instabilities in the laboratory. We interpret the results of experiments on this fault gouge analog in the context of modern theories of charge separation in geologic materials.

©2014. American Geophysical Union. All Rights Reserved.

2. Previous Work

2.1. Natural Occurrences

Light emissions have been reported in association with rock failure during both seismic rupture at Earth's surface (so-called Earthquake lights) and during rock bursts in mines. Earthquake lights have been reported during various stages of the seismic cycle, in addition to other electromagnetic phenomena. Related electrical phenomena believed to be connected with rock failure include ultralow frequency electromagnetic emissions, resistivity variations [*Park et al.*, 1993], and anomalous animal behavior [*Kirschvink*, 2000]. A summary of these phenomena by *Uyeda et al.* [2009, and references therein] illustrates the breadth of observations.

The first photographically well-documented sequence of earthquake lights (EQL) occurred during the 1965–1967 Matsushiro earthquake swarm [*Derr*, 1973]. Earthquake lights were also observed in the *M*7.2 29 November 1975 Kalapana earthquake. The *M*7.2 1995 Kobe earthquake was reported to have EQL as well as observations of burned plant roots at the rupture site and natural remanent magnetization (NRM) anomalies [*Enomoto and Zheng*, 1998]. Anomalous NRM have been measured in pseudotachylyte, suggesting that high remanent magnetizations were acquired in a coseismic electrical process and locked into thin, rapidly cooling layers of melt [*Ferré et al.*, 2005]. Visual electromagnetic phenomena were reported before the *M*6.3 6 April 2009 L' Aquila earthquake [*Fidani*, 2010]. Although reports were confused by astronomical/meteorological events and coseismic power line flashes, a number of unexplained observations remain.

Most reported EQL have been generated on intraplate faults with relatively shallow sources, for magnitude 7 and greater events, and commonly for earthquakes with demonstrated surface rupture. *Lockner et al.* [1983] suggest that vaporization of water produces a charge separation that is then moved to the surface by a central fluid conductor. Reports of EQL phenomena often include descriptions of the anomalies being most intense at topographic highs, suggesting that surface charge on the ground was concentrated by the topography. EQL may be more common in high stress drop events and/or in association with branching and geometrically complex events [*Scholz*, 2002].

2.2. Previous Experimental Work

Much experimental work has been done to test physical mechanisms that could cause electrical anomalies during seismic activity and rock failure. The most relevant explanations are briefly discussed here, but more in-depth discussion may be found in *Uyeda et al.* [2009], *Freund* [2000], and references therein.

Early work by *Nitsan* [1977] investigating piezoelectric effects showed electromagnetic radiation in the 1–10 MHz range during the fracturing of quartz-bearing rocks under uniaxial compression. The idea of the piezoelectric effect causing changes in the electrical field during failure suggested that frequency content of the signal would be related to the rate of stress release. This relationship is supported by a spectral shift to higher frequencies with smaller particles [*Nitsan*, 1977]. Uniaxial compression studies using cores of Red Texas Granite, Barre Granite, Dakota Sandstone, Carthage Marble, and quartzite exhibited electromagnetic signals peaking below 40 kHz in association with failure. Observed signals also exhibited some degree of directionality [*Rowell et al.*, 1981; *Hanson and Rowell*, 1982]. Signals peaking at 100 kHz were observed during impact and cratering tests by *Bianchi et al.* [1984] both in vacuum and at atmospheric pressure.

Mechanisms involving the formation of cold plasmas during fracture and impact have also been proposed to explain charge generation [*Martelli and Cerroni*, 1985] but have not been investigated thoroughly. Calculations considering a beam-plasma interaction producing an ion-acoustic instability suggest that the expected radiation frequencies are at ~50 kHz.

A recent study by *Onuma et al.* [2011] examined gabbro and quartz powders used as simulated fault gouge and sheared between gabbro forcing blocks in a saw cut geometry. Electrical signals in the coseismic period were detected by direct contact electrodes as well as toroidal induction coils surrounding the sample. In 25% of their experiments, a possible precursory signal was detected, but not consistently on all instruments. Piezoelectricity was ruled out as a dominant mechanism, because signals were observed in piezoelectric and nonpiezoelectric gouges and there was no preferred *c* axis orientation in the quartz powder. Signals were observed from piezoelectric and nonpiezoelectric materials by *Cress et al.* [1987] as well, but in their experiments on quartz produced larger signals than other materials. *Onuma et al.* [2011] did not observe signals during initial loading; however, such signals have been observed by other workers in natural and

©2014. American Geophysical Union. All Rights Reserved.

experimental cases [*Takeuchi et al.*, 2010] who attributed them to frictional electrification because they scaled roughly linearly with slip.

The presence of moving dislocations with respect to propagation of microcracks producing a "pressure-stimulated current" in marble samples has been examined [*Triantis et al.*, 2008]. These currents are a result of charge separation during the beginning stages of failure, not during the initial loading stages.

Piezoelectric effects are well-documented in materials such as quartz, but geologic materials are not expected to have the required mineralogy or grain alignment to make this a viable mechanism in nature. Randomly oriented grains would produce a series of randomly oriented dipoles that would cancel to produce a net-neutral field. Streaming potentials and electrokinetic effects [*Mizutani et al.*, 1976] are well-documented but are generally not of sufficient magnitude to explain the observed phenomena, because large potentials are difficult to maintain with generally conductive fluids present. Electrification by relative surface movement (triboelectrification) is also well-documented [*Pingali et al.*, 2009; *Pähtz et al.*, 2010] but does little to explain electrical signals produced while contacts are stationary to quasi-stationary.

Evidence for electrical signals during and possibly as precursors to failure in a low stress environment has been collected [*Shinbrot et al.*, 2012] in experiments examining slope failure and crack opening or closing in powdered pharmaceutical materials. An electrostatic voltmeter (ESVM) like that used in this study was used to monitor rotating and tilting drums of powder as well as flexure of powder layers resulting in opening and closing fissures of the material.

Another model of charge generation during deformation of geomaterials is the "semiconductor" effect. In geologic materials, oxygen is generally considered to exist in the O^{-2} valence state, but the more oxidized form O^{-} is also present in a pair of coupled O^{-} atoms known as a peroxy defect. The peroxy link can be broken via mechanical strain such as during passage of a mechanical deformation front in the form of a propagating elastic wave or elastodynamic rupture front. In this case, an electron is sourced in an attempt to satisfy the newly formed electrical imbalance at the site of the broken peroxy bond. This oxidizes the donor, forming a single-defect electron (equation (1)) [*Freund*, 2000; *Freund et al.*, 2006; *Freund*, 2010]

$$O_3X/^{OO}\backslash YO_3 + [XO_4]^{n-} \leftrightarrow O_3X/^{O}\bullet_{O}/YO_3 + [XO_4]^{(n-1)-}. \quad (1)$$

Electrons are not free as charge carriers, but holes remain mobile [*Freund*, 2000; *Freund et al.*, 2006; *Freund*, 2010; *Balk et al.*, 2009]. The semiconductor effect has been explored in solids [*Takeuchi and Nagao*, 2013; *St-Laurent et al.*, 2006], but few studies have been conducted on granular materials, which are likely to be important in the behavior of tectonic fault zones.

3. Methods

We conducted experiments on granular layers used to simulate fault gouge under controlled boundary conditions, with concurrent measurement of electrical potential, stresses, and strains of the layer to explore the relationship between stress state and the evolution of electrical signals. We used glass beads to represent granular fault gouge because they exhibit repeated frictional stick-slip behavior and share key friction constitutive properties with rock. The main advantage of this choice lies in the reproducibility of stick-slip behavior, allowing investigation and isolation of the processes that cause electrical signals relevant to natural faults containing granular gouge by using a simple, well-characterized system. We note that glass should contain fewer starting defects than silicate minerals found in natural fault gouges, such that any effects observed in our glass bead experiments would likely be amplified in natural materials.

3.1. Apparatus

All experiments were conducted on a biaxial deformation machine with a servo-hydraulic control system [*Karner and Marone*, 2000; *Frye and Marone*, 2002]. Hydraulic servo valves are operated in either displacement or force feedback modes through a series of analog amplifiers and comparators. Control displacement signals are generated by a 16 bit digital to analog converter capable of ±5V range. The apparatus (Figure 1a) is capable of 1 MN of force on the horizontal ram and 1.5 MN on the vertical ram. Ram velocity can be controlled to 0.1 μm/s in displacement mode or to about 10 N in load mode [*Hong and Marone*, 2005; *Rathbun et al.*, 2008].

©2014. American Geophysical Union. All Rights Reserved.

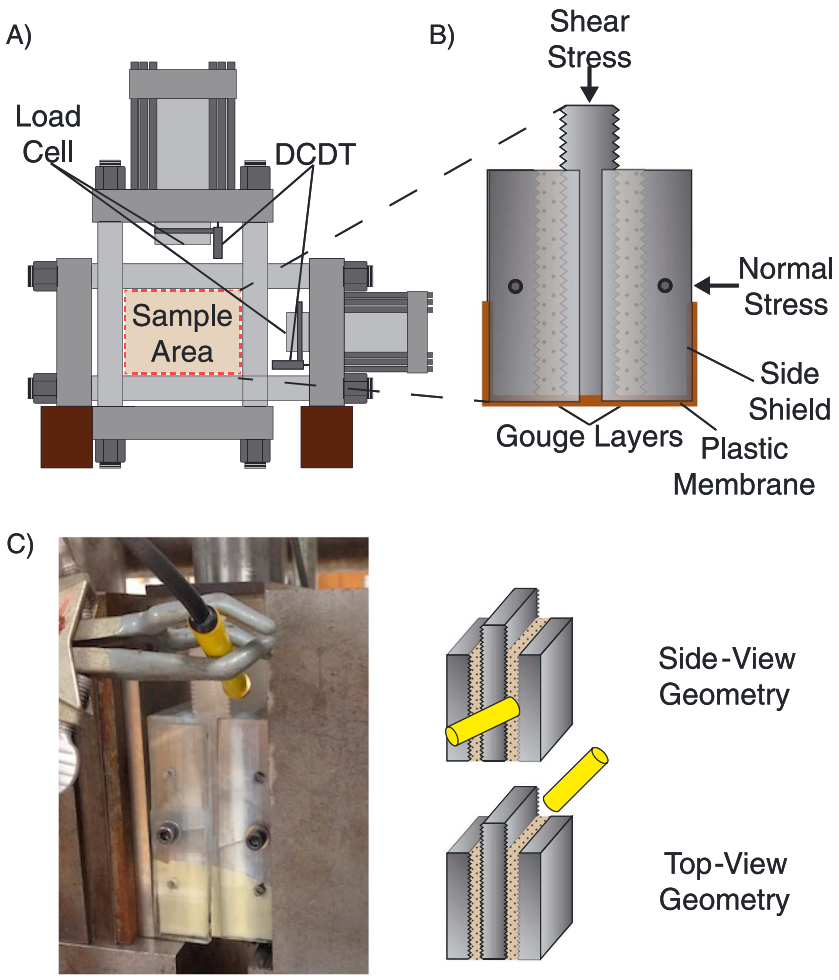

Figure 1. Experimental setup. (a) The biaxial hydraulic press: sample assemblies are supported by steel blocks in the sample area. (b) Double-direct shear geometry consists of two layers of gouge confined between three forcing blocks. Side shields and a plastic membrane are used to contain gouge material as the sample is sheared. (c) Placement of the electrostatic voltmeter (yellow cylinder) in the side- and top-view positions. A window was cut into the side shield for the side-view geometry.

We used forcing blocks of cast acrylic with a dielectric strength of 15–17 V/μm and a tensile strength of 55–77 MPa. Forcing blocks were cut to size and machined with grooves 1 mm deep and 2 mm wide perpendicular to the shearing direction to ensure that shear occurred within the layer and not at the layer boundary [*Anthony and Marone*, 2005; *Knuth and Marone*, 2007]. Acrylic side shields were also made to confine the sample material. The nominal frictional contact area was 10 cm ×10 cm.

Force was measured using Beryllium-Copper strain gauge load cells built in-house and placed in series with the loading ram and sample. The load cells and the wheatstone bridge electronics are calibrated regularly with a proving ring traceable to the National Bureau of Standards. Displacement is measured with direct current displacement transducers affixed to the ram nose and referenced to the end platens of the hydraulic rams. Positions of both classes of instrumentation are noted in Figure 1a.

We recorded data using a 24 bit, 16 channel simultaneous, delta-sigma style analog to digital system. Samples are collected at 10 kHz and averaged to the desired rate from 1 Hz to 10 kHz as necessary to maintain the appropriate signal-to-noise ratio. Recording rates may be changed during the experiment, and our tests show minimal cross talk or dwell errors in this system.

3.2. Sample Material and Preparation

Samples were built in the double-direct shear configuration (Figure 1b) using soda-lime glass beads [*Anthony and Marone*, 2005]. Two layers of beads were confined in a three forcing block assembly with a

©2014. American Geophysical Union. All Rights Reserved.

Table 1. List of Experiments

Experiment	V_{lp} (μm/s)	Bead Size (μm)	Temperature (C°)	Humidity (%)	Comment
p3853	30	420–500	23.3	41.2	Large beads
p3878	30	100–150	23.8	23.8	Side view
p3879	30	420–500	24.7	20.2	Large beads
p3880	30	420–500	25.7	20.7	Large beads
p3881	30	100–150	26.9	20.7	Side view
p3882	30	100–150	26.0	14.0	Side view
p3887	30	100–150	22.7	22.5	Side view
p3889	1	100–150	23.4	24.8	Side view
p3890	100	100–150	24.1	33.8	Side view
p3893	100	100–150	21.9	19.9	Side view
p3894	1	100–150	22.7	19.8	Side view
p4010	30	100–150	23.9	23.0	Top view-isolated ground
p4011	30	100–150	24.2	23.7	Top view
p4012	30	100–150	24.5	22.0	Top view
p4013	1	100–150	24.3	22.3	Top view
p4014	30	100–150	23.0	100	Saturated
p4015	30	100–150	23.3	N/A	Submerged
p4049	30	100–150	23.9	27.0	Control test
p4050	30	100–150	23.8	100	Saturated
p4051	30	100–150	23.9	N/A	Submerged
p4052	30	100–150	23.8	100	Saturated

rubber membrane at the bottom and side shields on the boundaries to avoid lateral extrusion of the material. The top of the sample was unconfined.

Layers were built by placing the side forcing blocks on a leveling jig and applying cellophane tape around the perimeter. The tape was then trimmed to the desired height to produce uniform, reproducible layers. We used 5 mm thick layers for all experiments in this study (Table 1). Sample material was poured into the form, lightly compacted, and leveled. The center forcing block was affixed to one side block (and the sample) with additional cellophane tape, securing the blocks and gouge layer and providing enough strength to allow transport of the sample from the bench to the deformation apparatus. The process is repeated for the second layer.

We constructed layers using Class IV soda-lime glass spheres (product GL0191B4/106-150) from Mo-Sci Specialty Products in Rolla, Missouri (composition shown in Table 2). Two monodisperse size distributions were tested: 100–150 μm and 420–500 μm. Scanning electron microscopy analysis of the beads shows that they are homogeneous, with few exceptions, and smooth (Figure 2). Past work has shown that bead comminution is minimal until $\sigma_n > 10$ MPa [*Mair et al.*, 2002; *Mair and Abe*, 2011].

Table 2. Composition of Glass Beads

Compound	Composition (%)
SiO_2	65–75%
Al_2O_3	0–5%
CaO	6–15%
MgO	1–5%
Na_2O	10–20%
Fe_2O_3	<0.8%

3.3. Potential Measurement

Electrical potential on the layers was measured by a model 344 noncontact electrostatic voltmeter (ESVM) manufactured by Trek Inc. This instrument reported the potential with respect to system ground sensed in its field of view. An analog output of the measured voltage was divided by 100 to provide a sensing range of ±2 kV with a ±20 VDC output signal recorded. A "response" setting on the instrument controlled internal damping constants.

The sensor head contains two electromechanically oscillated plates. Plates are fixed parallel to each other with the surface normal facing the surface under test. The front plate is affixed to the instrument body and has a small aperture in the center. The rear plate is inside

©2014. American Geophysical Union. All Rights Reserved.

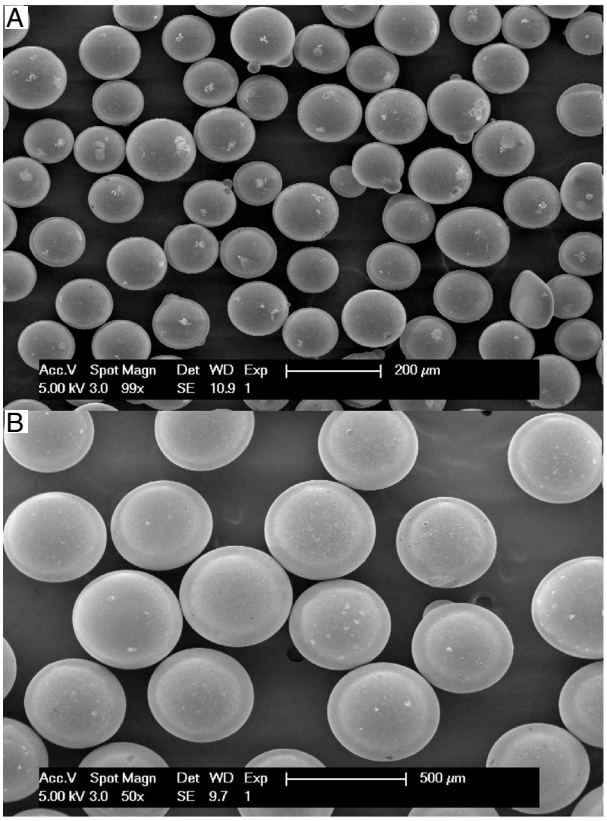

Figure 2. Scanning electron microscope micrographs of the starting glass beads for all experiments: (a) 100–150 μm and (b) 420–500 μm.

the instrument and is the oscillating plate. The sensor operates by varying the voltage across the plates and sensing the alternating current (AC) signal resulting from the movement of the plates with respect to one another. When the AC component of the signal is nulled, the voltage across the plates exactly matches the voltage on the surface under test. This sensor configuration has several advantages: (1) no contact is required with the surface under test, which is excellent for systems where coupling is a challenge, (2) there is no arcing risk since the instrument and surface under test are at the same potential, and (3) the sensor is easily portable, allowing tests with different viewing positions.

Two different sensor geometries were used: side view and top view (Figure 1c). In the top view, all tape between the sensor and the sample was removed. In the side view, a notch was cut in the side shield, leaving only a thin layer of tape (necessary to prevent extrusion) for the sensor to observe through. In our calibrations, we found that the sensor operates normally when viewing signals through thin obstacles.

3.4. Experimental Procedure

Samples were placed into the testing machine and normal load of 4 MPa was applied and maintained to compact the layers. The shear load was then applied by driving the vertical ram at a constant displacement rate (1, 30, or 100 μm/s). Electrical potential was recorded by placing the sensor in either the top- or side-view geometry with a distance of ~1 cm between the front of the sensor and the gouge layer. The response setting was set to the maximum value of 9.

We conducted experiments at room (ambient) humidity, at 100% relative humidity (RH), and under submerged conditions using de-aired water. The 100% RH was achieved by placing the sample assembly in a plastic membrane with a beaker of anhydrous sodium carbonate solution (2:1 ratio with distilled water) within the membrane. This exothermic reaction produced a 100% RH environment in the membrane. For all experiments under controlled humidity, samples were left to equilibrate overnight with a small normal stress applied by a hand clamp and then placed in the testing machine. When the experiment began, we refreshed the anhydrous sodium carbonate solution, applied the normal stress, and proceeded with our standard loading protocol. For these experiments, we cut a small window in the humidity-control membrane to provide access for the sensor. A capacitive sensor hygrometer (Lifft C200 with a maximum error of ±3%) verified that the relative humidity never fell below 100%. Saturated experiments were performed in a similar manner, but the membrane was filled with distilled water and the sample allowed to saturate as load was applied. The water level just covered the top of the blocks and a top-view ESVM geometry was employed.

3.5. Calibration and Control Tests

We performed tests to ensure calibration of the ESVM, as well as to evaluate the sensitivity of the response control. The ESVM probe was affixed to an electrically insulating base and placed approximately 1 cm from an aluminum plate. The plate was charged with a precision DC power supply (HP 6216B) and the true and

©2014. American Geophysical Union. All Rights Reserved.

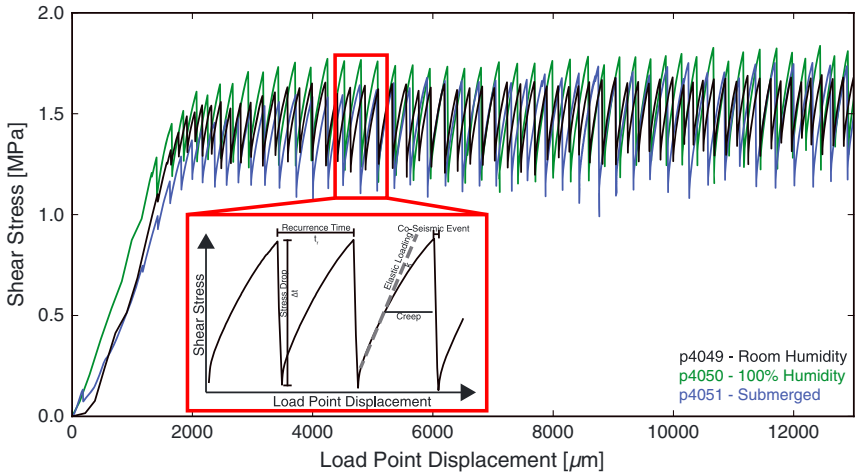

Figure 3. Experiments performed on glass beads (100–150 μm diameter) under ambient humidity, 100% humidity, and submerged conditions exhibit similar mechanical behavior. Increased stress drops are observed with increased humidity and in the submerged case. Inset: Anatomy of a stick-slip event. The recurrence time is the time between peaks in shear stress. Initially, the shear stress increases linear elastically. Deviation from line-elastic behavior marks the onset of elasto-plastic deformation and preseismic slip. When the ultimate strength of the layer is reached, shear stress drops rapidly and the cycle begins again.

measured plate voltages recorded. Performance was further evaluated by attaching the surface under test to a function generator. Square waves were measured on each response setting (1–9) to evaluate ringing of the instrument (Appendix A).

In addition, an experiment identical to those testing electrical potential on the layers was performed with the ESVM pointed away from the load frames into the room and toward a DC-charged aluminum plate. This test was performed to ensure that the signals we observed during shearing were not from electrical interference of the hydraulic control electronics or measurement/recording electronics. We note that our records include motion of the vertical hydraulic ram when it was not in contact with the sample, and no change in voltage was seen. This further indicates that no DC offsets or interference were experienced by the ESVM from the testing machine and/or control electronics and transducers.

All calibration and control tests were conducted with identical analog to digital conversion hardware as the experiments. ESVM calibration tests were also conducted on an independent logger (the LabJack U6) to ensure that there was consistent performance and minimal measurement burden from either system.

3.6. Data Analysis

Changes in electrical voltage during stick-slip events were picked by hand to evaluate the electrical signal. ESVM data are more noisy than the mechanical data, and electrical anomalies are not found with every stick-slip event, making manual picking the most accurate. Measured electrical potential and shear stress were plotted on the same *x* axis, and mouse position clicks were recorded. Interpretation was aided by superposition of a smoothed potential signal. The potential was smoothed using a Savitzky Golay filter [*Savitzky and Golay*, 1964], as it preserves peaks, but decreases noise. With the Savitzky Golay filter, a line of specified low order is fit to a certain data window using a linear least squares technique. The analysis is then stepped forward, and fit signals convolved.

Data were recorded in a binary form, decoded, converted from bits to engineering units through use of calibrations derived from our transfer standards, and then written out as either a binary or ASCII for analysis. The Python environment was used for processing and analysis. All stick-slip events were automatically picked by first computing the smoothed derivative of shear stress with respect to time using a running-average slope tool. Zero crossings of the derivative indicate a slope change from positive (like that during load up) to negative (like that during failure) or the reverse. The automatically determined stress drops were checked against a threshold value to ensure that no noise was picked as events. Automatic picks were visually inspected to ensure algorithm performance.

©2014. American Geophysical Union. All Rights Reserved.

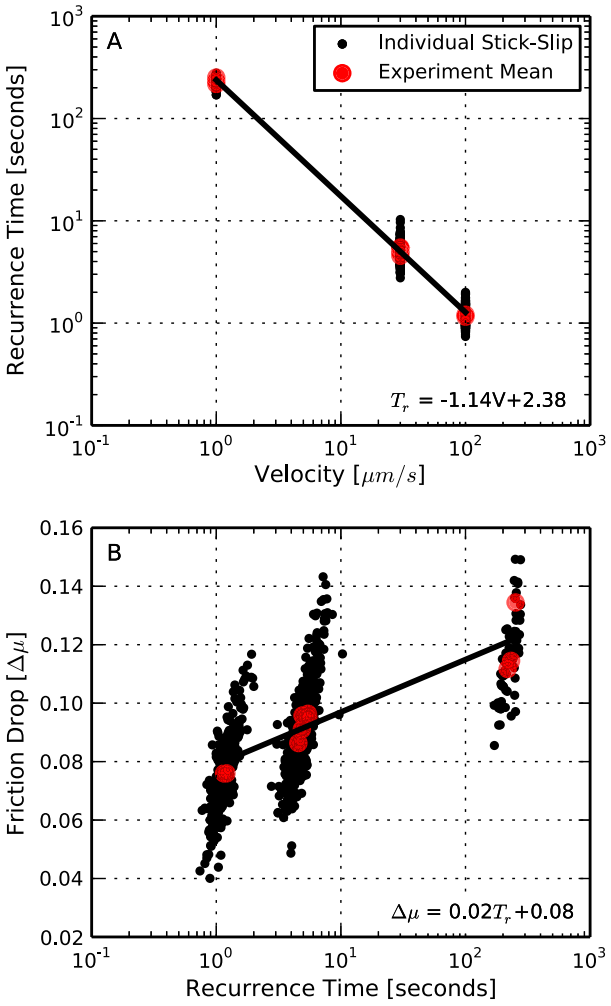

Figure 4. (a) Samples exhibit a log-log linear relation between recurrence time and velocity. Faster loading rates result in shorter recurrence times. (b) Friction drop increases with the recurrence time as there is more time for the layer to heal before the next stick-slip event.

4. Results

4.1. Mechanical Data

The application of shear load resulted in a characteristic linear-elastic stress-displacement record during initial run-in (Figure 3). Stick-slip behavior began as we reached the failure strength of the material. As shear load increased during the stick-slip cycle, the material began to creep and deform elastoplastically, as indicated by deviation of the stress-strain curve from the initial, linear-elastic trend. When the ultimate strength of the layer was reached, layers failed and a stress drop was observed. We define the stress drop as the magnitude of shear stress change during stick-slip failure. In a series of repeating events, we define the recurrence time as the time between peak stresses of two slip events. For a summary of this terminology, see Figure 3 inset. Mechanical steady state (not to be confused with steady state frictional sliding) refers to the system state after the initial run-in period, defined as the point at which stress drops in repeated stick-slip events become constant.

All experiments exhibited a maximum coefficient of friction during mechanical steady state ($\mu \equiv \tau/\sigma_n$) of 0.3–0.4. For experiments at 100% humidity or water saturated, we observed an increased stress drop and ultimate strength due to the activation of chemomechanical mechanisms such as solution-reprecipitation [*Frye and Marone*, 2002; *Yasuhara*, 2005; *Scuderi et al.*, 2014].

The recurrence time between events has been shown to vary with load point velocity [*Karner and Marone*, 2000; *Beeler et al.*, 2001]. We observe a power law relation between load point velocity and recurrence time with a characteristic slope of −1.14 (Figure 4a). For faster load point velocities, there is less time for contact healing to occur before the layer fails, resulting in lower maximum stresses and shorter recurrence times. Shorter healing times also result in smaller stress drops, which produce a correlation between longer recurrence times and larger stress drops (Figure 4b).

Experiments performed using the 420–500 μm glass beads exhibited repeated stick-slip behavior and a lower coefficient of friction of ~ 0.2–0.3. The occurrence of stick-slip events was less regular than that of the 100–150 μm experiments, as there were 5 times fewer beads spanning the same 5 mm layer thickness. For the larger beads, we conducted experiments only at 30 μm/s and we did not explore the role of loading velocity. Due to the large stresses applied to the acrylic forcing blocks by the large beads, some chipping of the grooves was observed, so no further experiments were conducted.

4.2. Electrical Data

During shearing we observe two common signals in the electrical potential. The first is characterized by a long period signal (lasting for the entire experiment) that is a general charging/discharging trend (Figure 5). The magnitude of this varies between experiments but can be as much as 250 V. The second is characterized by signals that are of smaller magnitude and shorter duration. These are superimposed on the long-term

©2014. American Geophysical Union. All Rights Reserved.

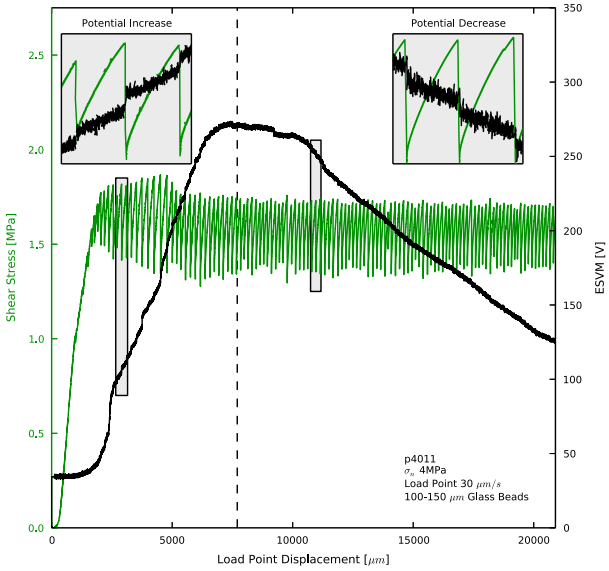

Figure 5. During shearing, two trends are observed: (1) a long-term charging/discharging trend in the electrical potential and (2) potential change related to individual stick-slip events. The entire system initially charges, approximately until mechanical steady state is reached. During this phase, coseismic potential changes are dominantly positive (top left inset). After attainment of mechanical steady state, the system begins to maintain or discharge potential. During this phase the co-seismic potential changes are dominantly negative (top right inset).

trend and are synchronous with individual stick-slip events. The polarity of these events (coseismic charging or discharging) varies systematically during an individual experiment. During the initial charging stage of the experiment, prior to reaching mechanical steady state sliding, the anomalies are generally positive. During the phase of overall discharging, the electrical anomalies coincident with stick slip are generally negative. There are occasional events of unexpected polarity, but there is a strong polarity preference based on the stage of the long-term trend. We consistently observed that the long-term charging/discharging trends were marked by the attainment of mechanical steady state (Figure 5).

After reaching mechanical steady state, the electrical anomalies associated with each stick-slip event varied systematically with loading velocity (Figure 6). For experiments subject to loading at 1 μm/s, voltage increased by 1–2 V during shear loading between stick-slip events and then dropped rapidly during coseismic failure. Similar behavior was observed at 30 μm/s, where voltage changes were 2–4 V. For shearing at 100 μm/s we found a change of electromechanical behavior. Initial loading still produced an increase of electrical potential, but during coseismic slip the potential spiked by tens of volts with the peak occurring just after the stress drop.

We found that the magnitude of potential change during stick-slip events follows a power law relationship with sliding velocity, resulting in an increase of about 5 times in voltage for the range of velocities we explored (Figure 7). For experiments at 100% RH (saturated) and submerged boundary conditions there was no regular electrical signal associated with the stick-slip events. Minor long-term charging/discharging trends were observed in some experiments.

Electrical anomalies were also observed in the three experiments run with larger (420–500 μm) grain size material. The anomalies were of similar nature and magnitude to those observed under identical conditions with the smaller grain size material.

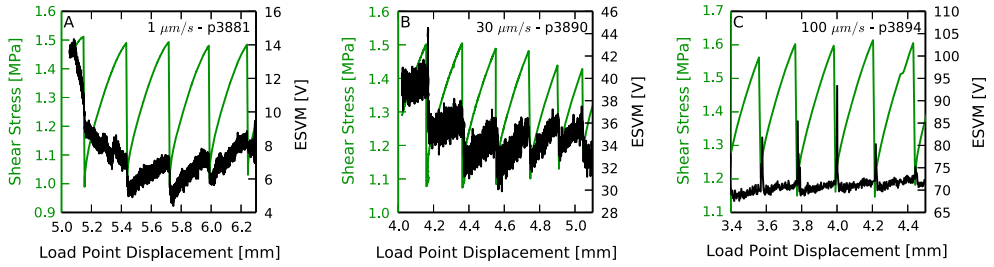

Figure 6. Stick-slip events and associated ESVM measurements for three different load point velocities of 1, 30, and 100 μm/s. (a) At slow loading velocities the electrical signal clearly mirrors the stress curve in most cases. (b) For intermediate velocities, the relation is still present. (c) At high velocities, the electrical signal is a sharp pulse, an order of magnitude higher than those observed at low velocities, and we observe small interseismic charging.

©2014. American Geophysical Union. All Rights Reserved.

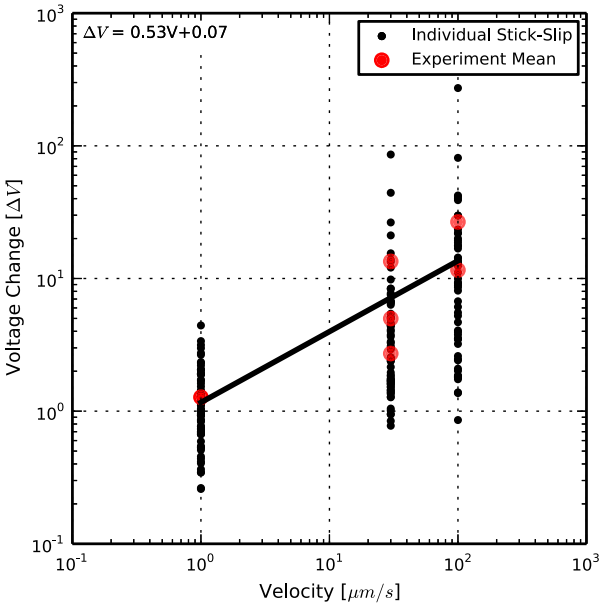

Figure 7. Each order of magnitude driving velocity change produces an ~5 times increase in the electrical signal observed. All experiments shown are with the side-view sensor geometry.

5. Discussion

One likely explanation for the electrical signals we observed during stick-slip events involves force chains and their role in the mechanical behavior of granular layers [*Majmudar and Behringer*, 2005]. Our experiments had no preferred *c* axis orientation of piezoelectric grains, ruling out the piezoelectric effect as a main contributor to the observed potentials. Likewise, vaporization of pore water cannot explain our data, because we observe coseismic signals in low humidity conditions. Streaming potentials are likewise not a major contributor in this configuration. Zeta potentials near individual grains are insufficient to explain the net external voltage we observed and would be expected to increase in the saturated and submerged conditions. The plasma model is not applicable to our conditions of low shear velocity and nonfracture experiments. Semiconductor effects and triboelectrification/contact electrification are two possible mechanisms operating in our experiments; each has the capability to create a potential gradient within the sheared granular samples. Broadly, semiconductor effects are stress-dependent mechanisms and triboelectric effects are displacement-dependent phenomena.

We note that cellophane tape was used in our experiments and that it is electrically active [*Camara et al.*, 2008]. However, based on our calibrations and from tests with no tape, we believe that this is not responsible for the signals we observe. Elastic strains in the forcing blocks, where the tape is attached, are low, and signals are observed when the system is stationary to quasi-stationary during elastic loading. Also, the observed change of sign, from charging to discharging is not consistent with signals from a single mechanism (tape peeling). Finally, we also observed very similar signals from a top-viewing geometry with no tape between the sensor and the layer.

Our experiments consider a fault zone on the order of 10 cm in length. This presents a potential challenge in upscaling our observations to natural fault zones. Additionally, the electrical potentials generated in our experiments are much smaller than those required to explain most field observations, and our measurements were conducted with direct access to the fault zone. One possible explanation is the low number of defects likely to be present in industrially produced glass versus natural silicate minerals.

5.1. Electromechanical Model

We hypothesize that the shear load across our granular layers is supported primarily by a small percentage of grains that form layer-spanning chains of highly stressed particles. Granular force chains produce a "fragile" configuration and are separated by regions of spectator grains that support little to no load [*Sammis et al.*, 1987; *Liu et al.*, 1995; *Liu and Nagel*, 1998; *Cates et al.*, 1998; *Boettcher*, 1999; *Albert et al.*, 2001; *Aharonov and Sparks*, 1999].

The observation that the overall electrical signal consists of two parts, charging and discharging, suggests that two mechanisms may be responsible for our observations. The long-term charging trend ceases at approximately the same time as the system reaches mechanical steady state, suggesting a dependence on the mechanical evolution of the layers. During the initial load up of the system, there is large-scale grain rearrangement as force chain networks form and the layers compact. This grain rearrangement involves enhanced grain boundary sliding that can triboelectrically charge the system (Figure 8a). The acrylic forcing blocks will hold surface charge, but the charge will slowly drain through various sinks, including contact with the metal loading platens. After a mature force chain network is formed, interparticle movement and

©2014. American Geophysical Union. All Rights Reserved.

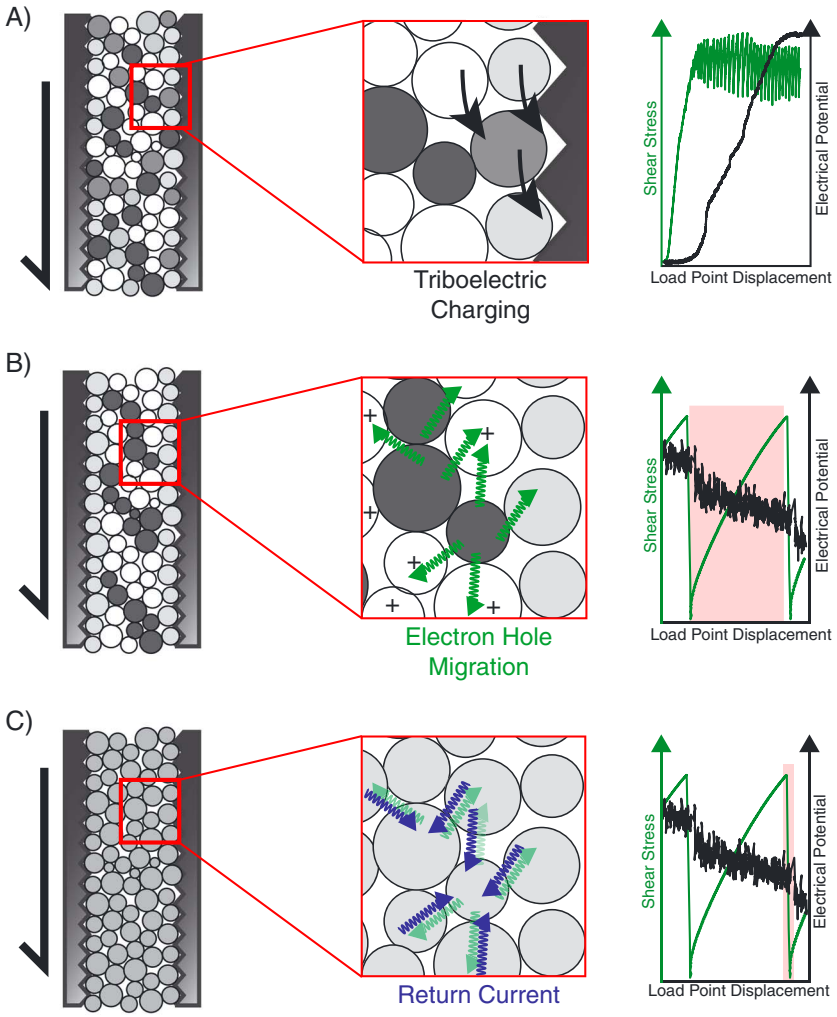

Figure 8. A schematic representation of the stages of electrical behavior during an experiment: (a) During the initial run-in, there is massive grain rearrangement as force chain networks begin to form. This sliding motion triboelectrically charges the system. (b) After the force chain network forms, there is minimal grain boundary sliding. Shear loads are supported in the granular layer by highly stressed force chains (dark colors). Electron holes migrate away from highly stressed beads into the matrix creating an electrical potential gradient. (c) When the layer fails and all grains are at roughly the same low stress, a return current redistributes the electrical gradient and the cycle begins again.

grain boundary sliding at the forcing block interface are minimal, which would reduce charging of the forcing blocks. We posit that at this point the rate of discharge becomes equal to or greater than the rate of triboelectric charging, resulting in long-term discharging.

After the system reaches mechanical steady state behavior, we expect a network of force chains to support the load during the loading portion of the stick-slip cycle. Grains involved in supporting the load experience much higher local stresses than the spectator grains or the bulk stress measured on the layer. Any electron defects in the highly stressed grains will migrate to less stressed grains adjacent to the force chain. Grains involved in a force chain will be at a lower potential (thus serving as acting anodes) than the spectator grains that are now enriched in positive charge carriers (thus acting as cathodes). This would result in the net measurement of a positive potential that increases with the shear load (Figure 8b).

When the force chain network can no longer support the applied load, the chains fail, resulting in stick-slip and returning the grains (temporarily) to a more homogeneous stress state. The resulting return current redistributes the potential, producing the observed net drop of potential on the layer during stick-slip failure (Figure 8c).

©2014. American Geophysical Union. All Rights Reserved.

The nature of the sharp positive potential spikes just after coseismic slip in the 100 μm/s driving velocity case remains unexplained by our conceptual model, but the coincidence of the spike with the time during which grains are moving suggests a dominating triboelectric mechanism at high load point velocities.

Coseismic charging events observed during the initial loading and first few stick slips of the experiments appear to be related to the attainment of mechanical steady state. As the force gradient driving the electrical potential is released during the coseismic slip, it is possible that instead of neutralizing the charge on layers that the charge follows, a second electromotive gradient to the initially lower potential side blocks. This results in an increase in the net potential to ground in the viewing area of the instrument. It is also possible that the rapid charging is a result of triboelectric effects with boundaries during grain rearrangement as the slip occurs before the force chain network is established. The lack of coseismic charging events during the bulk system discharging phase after steady state supports the latter hypothesis.

We note that the 100% RH experiments and the experiments where layers were submerged produced no consistent electrical signals. These experiments showed hints of the long-term potential variations, similar to the charging and discharging trends observed in ambient humidity experiments, but never over 50 V during the course of an experiment. In such moist environments, where conductivity is expected to be high, electrical potential gradients are difficult to maintain without a significant forcing mechanism. The high mobility of electrons in water would allow charge to move; in contrast, holes are not easily mobile in water, further reducing the potential gradient [*Balk et al.*, 2009].

6. Conclusions

We show that reproducible electrical potential anomalies can be observed during laboratory shear experiments and are associated with repeated stick-slip failure events. The test material of soda-lime beads allows a well-controlled study and is geologically relevant to faults containing granular gouge. We propose that our observations may be explained by a combination of the semiconductor effect, triboelectric charging, and a force chain model of loading in granular materials.

The results of this study suggest that small precursory stress drops (foreshocks) in nature may produce electromagnetic signals that could be used as an early warning mechanism for large earthquakes. Such signals would provide more warning than current methods, even if associated with the main shock because of their velocity of propagation. Even in rock, the electromagnetic signal produced by a time-variant electrical field would propagate at many times the elastic *P* wave velocity, producing seconds of warning for observers sufficiently far away. Our research may also find application in mines with relation to wall and column failure and in slope failure research. In those cases, an understanding of the electrical signals produced could lead to the design of optimum receiver location and improved processing methods, which would increase warning time of natural disasters.

We note that questions about charge conduction to the surface in earthquake faulting, upscaling of laboratory experiments, and the nature of the charge release through the earth-atmosphere system, remain unexplained. Complex resistivity and the frequency dependence of resistivity are likely important in natural systems. Further investigations of the natural observations and of how chemistry of the material and pore waters influences charge generation are necessary. Similarities in fault zones with reported observations may provide clues, but such observations are rare and generally poorly instrumented. Establishing small sensor networks of visual, spectral, and electromagnetic instruments is crucial to documenting the phenomena and beginning to understand its potential for early warning.

Future experiments will attempt to measure the flow of electrons to and from system ground required to hold the entire system at zero potential in contrast to the presented experiments, in which we isolate the system and measured the resulting potential. This technique allows conductive forcing blocks to be used, making contact with the entire layer and eliminating charging concerns. Spectral characterization of the electrical signals may also provide further insight into the charging mechanism.

©2014. American Geophysical Union. All Rights Reserved.

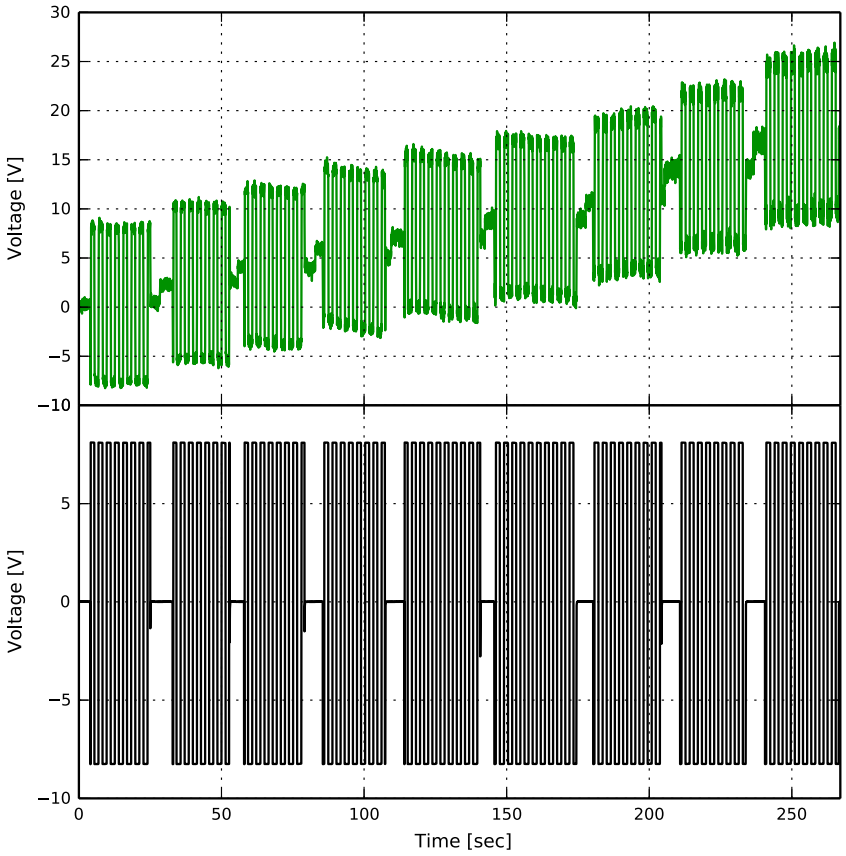

Figure A1. (bottom) Calibration of the ESVM from a function generator source. (top) A series of steps through the ESVM response setting from 1 to 9 show that the input square wave applied to the aluminum surface under test is well recorded on each setting. The upward trend in ESVM data is a product of a DC offset that occurs each time the response setting is changed on the instrument.

Appendix A: ESVM Calibration

The electrostatic voltmeter (ESVM) from Trek is a relatively new method of noncontact surface potential measurement and has not been applied in rock mechanics studies before. To gain confidence in the instrument, a series of tests were conducted by mounting the instrument to a set of nonconductive granite blocks with an adhesive backed paper tape as a bench-top jig. An aluminum plate of 5 cm diameter was placed 1 cm from the aperture of the probe (which has a viewing area of approximately 1:5 according to the manufacturer).

Constant DC voltages, stepped DC patterns, and a square wave pattern were utilized to check the response time of the instrument, calibrate the use of the response setting, and to ensure there was negligible cross talk between channels on the analog to digital converter. The input signal (true) to the plate was recorded simultaneously with the ESVM measured voltage for each of the 9 response settings (Figure A1). DC offsets during this calibration come from changing the setting on the instrument. For all settings the power was not cycled, and the instrument probe remained stationary.

Recorded waveforms at low response show smoothing of the sharp edges of the square wave. High-response waveforms do not exhibit smoothing or ringing, but in both cases the waveform rapidly reaches the correct voltage (Figure A2). High-response waveform recordings are more noisy but share the mean of the smoothed waveforms. All waveform leading/falling edges corresponded well with changes in the input signal in the time domain (Figure A3).

©2014. American Geophysical Union. All Rights Reserved.

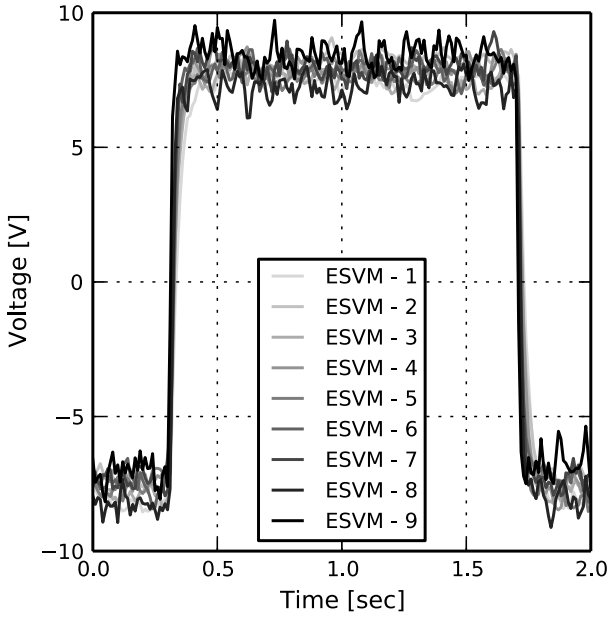

Figure A2. A detailed comparison of a single waveform shows that at lower response settings (lighter colors) the waveform is smoothed slightly, with the nearly instantaneous voltage change distributed over up to 0.1 s on both the rise and fall. At higher resolutions (darker colors) the sharp transition is clearly seen, but at the price of a higher noise level during the flat hold states.

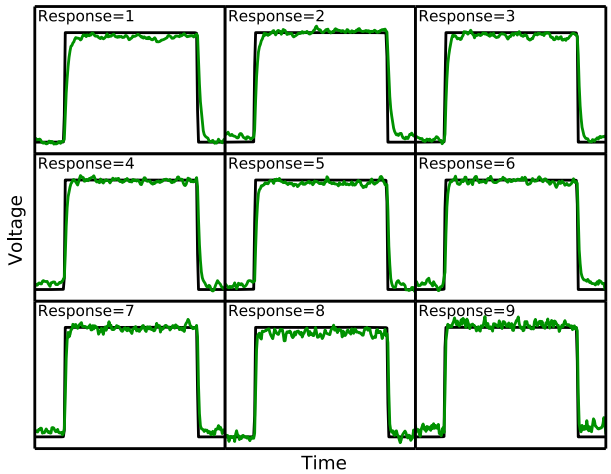

Figure A3. At all response settings the beginning of ESVM signal change corresponds well in the time domain with the leading and falling edge of the input signal. Smoothing due to longer integration times is observed at low response settings.

©2014. American Geophysical Union. All Rights Reserved.

Acknowledgments
The authors wish to thank F. Freund, Eric Ferré, and Max Meju for reviews that greatly contributed to the quality of the manuscript. This work was supported by NSF grants OCE-0648331, EAR-0746192, EAR-1045825, EAR-0950517, the GDL Foundation, and the Penn State University Graduate Fellowship. The presented data are available via FTP transfer by contacting the authors.

References

Aharonov, E., and D. Sparks (1999), Rigidity phase transition in granular packings, *Phys. Rev. E*, *60*(6), 6890–6896.
Albert, I., J. Sample, A. Morss, S. Rajagopalan, A.-L. Barabási, and P. Schiffer (2001), Granular drag on a discrete object: Shape effects on jamming, *Phys. Rev. E*, *64*(6), 061,303.
Anthony, J. L., and C. Marone (2005), Influence of particle characteristics on granular friction, *J. Geophys. Res.*, *110*, B08409, doi:10.1029/2004JB003399.
Balk, M., M. Bose, G. Ertem, D. A. Rogoff, L. J. Rothschild, and F. T. Freund (2009), Oxidation of water to hydrogen peroxide at the rock–water interface due to stress-activated electric currents in rocks, *Earth Planet. Sci. Lett.*, *283*(1), 87–92.
Beeler, N. M., S. H. Hickman, and T.-f. Wong (2001), Earthquake stress drop and laboratory-inferred interseismic strength recovery, *J. Geophys. Res.*, *106*(B12), 30,701–30,713.
Bianchi, R., F. Capaccioni, P. Cerroni, M. Coradini, E. Flamini, P. Hurren, G. Martelli, and P. N. Smith (1984), Radiofrequency emissions observed during macroscopic hypervelocity impact experiments, *Nature*, *308*(5962), 830–832.
Boettcher, M. S. (1999), Numerical simulations of granular shear zones using the distinct element method 1. Shear zone kinematics and the micromechanics of localization, *J. Geophys. Res.*, *104*(B2), 2703–2719.
Camara, C. G., J. V. Escobar, J. R. Hird, and S. J. Putterman (2008), Correlation between nanosecond X-ray flashes and stick–slip friction in peeling tape, *Nature*, *455*(7216), 1089–1092.
Cates, M., J. Wittmer, J.-P. Bouchaud, and P. Claudin (1998), Jamming, force chains, and fragile matter, *Phys. Rev. Lett.*, *81*(9), 1841–1844.
Cress, G. O., B. T. Brady, and G. A. Rowell (1987), Sources of electromagnetic radiation from fracture of rock samples in the laboratory, *Geophys. Res. Lett.*, *14*(4), 331–334.
Derr, J. S. (1973), Earthquake lights: A review of observations and present theories, *Bull. Seismol. Soc. Am.*, *63*(6), 2177–2187.
Dickinson, J. T. (1982), Fracto-emission accompanying adhesive failure, *J. Vac. Sci. Technol.*, *20*(3), 436, doi:10.1116/1.571327.
Dickinson, J. T., L. C. Jensen, and A. Jahan-Latibari (1984), Fracto-emission: The role of charge separation, *J. Vac. Sci. Technol. A*, *2*(2), 1112–1116.
Dickinson, J. T., L. C. Jenson, and M. K. Park (1982), Time-of-flight measurements of the mass-to-charge ratio of positive ion emission accompanying fracture, *J. Mater. Sci.*, *17*(11), 3173–3178.
Enomoto, Y., and Z. Zheng (1998), Possible evidences of earthquake lightning accompanying the 1995 Kobe earthquake inferred from the Nojima fault gouge, *Geophys. Res. Lett.*, *25*(14), 2721–2724.
Ferré, E. C., M. S. Zechmeister, J. W. Geissman, N. MathanaSekaran, and K. Kocak (2005), The origin of high magnetic remanence in fault pseudotachylites: Theoretical considerations and implication for coseismic electrical currents, *Tectonophysics*, *402*(1-4), 125–139.
Fidani, C. (2010), The Earthquake Lights (EQL) of the 6 April 2009 Aquila earthquake, in Central Italy, *Nat. Hazards Earth Syst. Sci.*, *10*, 967–978.
Finkelstein, D., R. D. Hill, and J. R. Powell (1973), The piezoelectric theory of earthquake lightning, *J. Geophys. Res.*, *78*(6), 992–993.
Freund, F. (2000), Time-resolved study of charge generation and propagation in igneous rocks, *J. Geophys. Res.*, *105*(B5), 11,001–11,019.
Freund, F. (2010), Toward a unified solid state theory for pre-earthquake signals, *Acta Geophys.*, *58*(5), 719–766.
Freund, F. T., A. Takeuchi, and B. W. S. Lau (2006), Electric currents streaming out of stressed igneous rocks: A step towards understanding pre-earthquake low frequency EM emissions, *Phys. Chem.*, *31*(4-9), 389–396.
Frid, V., D. Bahat, J. Goldbaum, and A. Rabinovitch (2000), Experimental and theoretical investigations of electromagnetic radiation induced by rock fracture, *Isr. J. Earth Sci.*, *49*, 9–19.
Frye, K. M., and C. Marone (2002), Effect of humidity on granular friction at room temperature, *J. Geophys. Res.*, *107*(B11), 2309, doi:10.1029/2001JB000654.
Hanson, D. R., and G. A. Rowell (1982), *Electromagnetic Radiation From Rock Failure*, Bureau of Mines Report of Investigations, Washington, D. C.
Hong, T., and C. Marone (2005), Effects of normal stress perturbations on the frictional properties of simulated faults, *Geochem. Geophys. Geosyst.*, *6*, Q03012, doi:10.1029/2004GC000821.
Jouniaux, L., and T. Ishido (2013), Electrokinetics in Earth sciences, *Int. J. Geophys.*, *2013*, 419,854, doi:10.1155/2013/419854.
Karner, S. L., and C. Marone (2000), Effects of loading rate and normal stress on stress drop and stick-slip recurrence interval, in *Geocomplexity and the Physics of Earthquakes*, vol. 120, edited by J. B. Rundle, D. L. Turcotte, and W. Klein, pp. 187–198, AGU, Washington, D. C.
Kirschvink, J. L. (2000), Earthquake prediction by animals: Evolution and sensory perception, *Bull. Seismol. Soc. Am.*, *90*(2), 312–323.
Knuth, M., and C. Marone (2007), Friction of sheared granular layers: Role of particle dimensionality, surface roughness, and material properties, *Geochem. Geophys. Geosyst.*, *8*, Q03012, doi:10.1029/2006GC001327.
Liu, A. J., and S. R. Nagel (1998), Nonlinear dynamics: Jamming is not just cool any more, *Nature*, *396*(6706), 21–22.
Liu, C.-h., S. R. Nagel, D. A. Schecter, S. N. Coppersmith, S. Majumdar, O. Narayan, and T. A. Witten (1995), A model for force fluctuations in bead packs, *Science*, *269*, 513–515.
Lockner, D. A., M. Johnston, and J. D. Byerlee (1983), A mechanism to explain the generation of earthquake lights, *Nature*, *302*, 28–33.
Mair, K., and S. Abe (2011), Breaking up: Comminution mechanisms in sheared simulated fault gouge, *Pure Appl. Geophys.*, *168*(12), 2277–2288.
Mair, K., K. M. Frye, and C. Marone (2002), Influence of grain characteristics on the friction of granular shear zones, *J. Geophys. Res.*, *107*(B10), 2219, doi:10.1029/2001JB000516.
Majmudar, T. S., and R. P. Behringer (2005), Contact force measurements and stress-induced anisotropy in granular materials, *Nature*, *435*(1079), 1079–1082.
Martelli, G., and P. Cerroni (1985), On the theory of radio frequency emission from macroscopic hypervelocity impacts and rock fracturing, *Phys. Earth Planet. Inter.*, *40*(4), 316–319.
Mizutani, H., T. Ishido, T. Yokokura, and S. Ohnishi (1976), Electrokinetic phenomena associated with earthquakes, *Geophys. Res. Lett.*, *3*(7), 365–368.
Nitsan, U. (1977), Electromagnetic emission accompanying fracture of quartzłbearing rocks, *Geophys. Res. Lett.*, *4*(8), 333–336.
Onuma, K., J. Muto, H. Nagahama, and K. Otsuki (2011), Electric potential changes associated with nucleation of stick-slip of simulated gouges, *Tectonophysics*, *502*(3-4), 308–314.
Pähtz, T., H. J. Herrmann, and T. Shinbrot (2010), Why do particle clouds generate electric charges?, *Nat. Phys.*, *6*(5), 364–368.
Park, S. K., M. J. S. Johnston, T. R. Madden, and F. Dale Morgan (1993), Electromagnetic precursors to earthquakes in the ULF band: A review of observations and mechanisms, *Rev. Geophys.*, *31*(2), 117–132.
Pingali, K. C., T. Shinbrot, S. V. Hammond, and F. J. Muzzio (2009), An observed correlation between flow and electrical properties of pharmaceutical blends, *Powder Technol.*, *192*(2), 157–165.

©2014. American Geophysical Union. All Rights Reserved.

Rathbun, A. P., C. Marone, R. B. Alley, and S. Anandakrishnan (2008), Laboratory study of the frictional rheology of sheared till, *J. Geophys. Res.*, *113*, F02020, doi:10.1029/2007JF000815.

Rowell, G. A., B. T. Brady, L. P. Yoder, and D. R. Hanson (1981), Precursors of laboratory rock failure, in *Fracture Mechnanics for Ceramics, Rocks, and Concrete*, edited by S. W. Freiman and E. R. Fuller, pp. 196–220, ASTM, Philadelphia, Pa.

Sammis, C., G. King, and R. Biegel (1987), The kinematics of gouge deformation, *Pure Appl. Geophys.*, *125*(5), 777–812.

Savitzky, A., and M. J. E. Golay (1964), Smoothing and differentiation of data by simplified least squares procedures, *Anal. Chem.*, *36*(8), 1627–1639, doi:10.1021/ac60214a047.

Scholz, C. H. (2002), *The Mechanics of Earthquakes and Faulting*, Cambridge Univ. Press, New York.

Scuderi, M., B. Carpenter, and C. Marone (2014), Physicochemical processes of frictional healing: Effects of water on stick-slip stress drop and friction of granular fault gouge, *J. Geophys. Res. Solid Earth*, doi:10.1002/2013JB010641, in press.

Shinbrot, T., N. H. Kim, and N. N. Thyagu (2012), Electrostatic precursors to granular slip events, *Proc. Natl. Acad. Sci. U.S.A.*, *109*(27), 10,806–10,810.

St-Laurent, F., J. S. Derr, and F. T. Freund (2006), Earthquake lights and the stress-activation of positive hole charge carriers in rocks, *Phys. Chem. Earth*, *31*(4-9), 305–312.

Takeuchi, A., and T. Nagao (2013), Activation of hole charge carriers and generation of electromotive force in gabbro blocks subjected to nonuniform loading, *J. Geophys. Res. Solid Earth*, *118*(3), 915–925, doi:10.1002/jgrb.50111.

Takeuchi, A., Y. Futada, K. Okubo, and N. Takeuchi (2010), Positive electrification on the floor of an underground mine gallery at the arrival of seismic waves and similar electrification on the surface of partially stressed rocks in laboratory, *Terra Nova*, *22*(3), 203–207.

Triantis, D., C. Anastasiadis, and I. Stavrakas (2008), The correlation of electrical charge with strain on stressed rock samples, *Nat. Hazards Earth Syst. Sci.*, *8*, 1243–1248.

Uyeda, S., T. Nagao, and M. Kamogawa (2009), Short-term earthquake prediction: Current status of seismo-electromagnetics, *Tectonophysics*, *470*(3), 205–213.

Yasuhara, H. (2005), Fault zone restrengthening and frictional healing: The role of pressure solution, *J. Geophys. Res.*, *110*(B6), B06310, doi:10.1029/2004JB003327.

©2014. American Geophysical Union. All Rights Reserved.